

Supplementary Information

**Observation of reactive intermediates in the initial stage during ethene
conversion over acidic zeolites**

Jing Niu^a, Yu-Ting Miao^a, Wei David Wang^a, Meng-Tong Ruan^a, Zhi-Peng Wang^a, Hua-Dong Xue^a, Si-Min
Yu^{*a}, Chong Liu^{*b}, Jian-Feng Wu^{*a}, and Wei Wang^{*a}

^a *State Key Laboratory of Applied Organic Chemistry, College of Chemistry of Chemical Engineering,
Lanzhou Magnetic Resonance Center, Lanzhou University, Lanzhou, Gansu 730000, P. R. China.*

^b *State Key Laboratory of Structural Chemistry, Fujian Institute of Research on the Structure of Matter,
Chinese Academy of Science, Fuzhou, Fujian 350002, P. R. China.*

Contents

A. Experimental procedures	S3
B. Characterization of zeolite H-Y	S6
C. Conversion of ethene on zeolite H-Y	S8
D. Identification of hydrocarbon products during conversion of ethene	S9
E. Conversion of ethene on zeolite H-SAPO-34	S11
F. Preparation of SES by dehydration of ethanol on zeolite H-Y	S12
G. ^{13}C scrambling of SES on zeolite H-Y	S13
H. ^{13}C isotropic distributions in $\text{C}_2\text{--C}_5$ hydrocarbons	S15
I. Analysis of zeolite-trapped organics after decomposition of SES	S17
J. Continuous-flow experiments for conversion of ethene on zeolite H-Y	S18
K. Overall mechanism for conversion of ethene to hydrocarbons	S19
L. DFT study on conversion of ethene into surface <i>n</i> -butoxy species	S20
M. References	S24

A. Experimental procedures

Materials. Zeolite Na-Y (Si/Al ratio of 5) was purchased from the Catalyst Plant of Nankai University, Tianjin, P. R. China. ^{13}C -1-Labeled ethanol (^{13}C -enrichment of 99%), ^{13}C -2-labeled ethanol (^{13}C -enrichment of 99%), and ^{13}C -labeled ethene (^{13}C -enrichment of 99%) were purchased from Cambridge Isotopes. All of the ^{13}C -labeled reagents were degassed via three “freeze-pump-thaw” cycles before use. Ethene (99.99%) was purchased from Hebei Qiming New Energy Technology Co., Ltd., and used as received without further purification. All other reagents used were of analytical grade.

Sample preparation. The $\text{NH}_4\text{-Y}$ zeolite was prepared via a five-fold ion-exchange of zeolite Na-Y at 353 K in a 1.0 M aqueous solution of NH_4NO_3 . Subsequently, the $\text{NH}_4\text{-Y}$ zeolite was heated up to 743 K under evacuation and was maintained at this temperature for 45 h, leading to zeolite H-Y.

Isotope labeling experiments. Selectively ^{13}C -labeled surface ethoxy species (SES) were prepared by the dehydration of ^{13}C -1-labeled or ^{13}C -2-labeled ethanol on zeolite H-Y on a vacuum line at 403 K for 12 h. In this work, the C_2 reactant (ethene or surface ethoxy species) along with catalyst is sealed in a glass ampoule, similar to the reaction condition in a batch reactor. The C_2 reactant adsorbed on zeolite H-Y were transferred into a glass ampoule in a glove box and then flame-fused on a vacuum line. After being heated at a given temperature (443 K to 473 K) within a given reaction time (0.5 h to 6.0 h), the sealed sample was broken within a liquid nitrogen bath, and then immediately transferred into an NMR rotor for solid-state NMR (ssNMR) measurements. Afterwards, the NMR rotor was opened and transferred to a headspace bottle under a liquid nitrogen bath in a glove box. The gaseous products in the headspace bottle were directly injected into the GC-MS at room temperature with a volume of 1 mL. The recycled sample was then transformed into a centrifuge tube. Subsequently, 30 mg of the sample was dissolved in 1 mL of 10 % HF solution for 10 min. The zeolite-trapped organics were further extracted using 1 mL of CH_2Cl_2 and subjected to GC-MS analysis. All the data were taken from the independent experiments with paralleling samples.

ssNMR measurements. All 1D MAS NMR measurements were performed with a 4 mm MAS NMR probe on a Bruker Avance II WB 400 MHz spectrometer at resonance frequencies of 400.1, 100.6, 104.3, and 79.5 MHz for ^1H , ^{13}C , ^{27}Al , and ^{29}Si , respectively. The sample spinning rate was set as 10.0 kHz. ^1H MAS NMR spectra were performed with a $\pi/2$ excitation of 3.53 μs and a repetition time of 5 s. ^{13}C CP MAS NMR spectra were recorded with a contact time of 3 ms and a repetition time of 2 s. ^{13}C HPDEC MAS NMR spectra were recorded after an excitation with $\pi/2$ pulse of 5.0 μs and a repetition time of 3 s. ^{27}Al MAS NMR spectra were performed with a $\pi/12$ excitation of 0.45 μs and a repetition time of 0.5 s. ^{29}Si MAS NMR spectra were performed with a $\pi/2$ excitation of 7.5 μs and a repetition time of 30 s. The chemical shifts in the ^1H , ^{13}C and ^{29}Si NMR spectra were referenced to tetramethylsilane (TMS) and the ^{27}Al chemical shifts were referenced to 1.0 M aqueous solution of $\text{Al}(\text{NO}_3)_3$.

The 2D ^{13}C - ^1H HETCOR (heteronuclear correlation spectroscopy), ^{13}C - ^{13}C refocused INADEQUATE

(incredible natural abundance double quantum transfer experiment) spectra, and 2D ^{13}C - ^{13}C CORD (combined R2-driven) spin diffusion spectra were performed with a 4 mm probe on a Bruker Avance NEO WB 600 MHz spectrometer with a sample spinning rate of 12 kHz. 2D HETCOR spectroscopy can be used to explore the spatial proximities of heteronuclei ^{13}C and ^1H . The ^{13}C - ^1H HETCOR spectrum was obtained using the ^1H - ^{13}C CP period of 3 ms with the recycle delay of 2 s, acquisition times of 26 ms (F2, ^{13}C) and 10 ms (F1, ^1H), and the number of scans of 360. INADEQUATE spectroscopy can be used to detect the homonuclear correlations via through-bond spin-spin couplings. The INADEQUATE spectra were recorded the ^1H - ^{13}C CP period of 3 ms with a recycle delay of 3 s. A total of 256 t1 FIDs were recorded at increments of 2.5 ms. The 2D ^{13}C - ^{13}C CORD spectrum was recorded with the a recycle delay of 2 s, and a spin diffusion mixing time of 50 ms.

GC-MS analysis. All samples were analyzed by Thermo Fisher Ultra Trace DSQ II GC-MS analyzer equipped with a capillary column and a mass detector (Thermo Fisher DSQ II) using an ionization voltage of 70.0 eV and a source temperature of 503 K. The gaseous products were analyzed by GC-MS analyzer equipped with a CP-7348 capillary column (25 m \times 0.25 mm \times 0.30 μm); the oven temperature was programmed from an initial temperature of 305 K for 3 min to a final temperature of 473 K for 6 min with a heating rate of 10 K/min. The zeolite-trapped organics were analyzed by GC-MS analyzer equipped with a DB-5 MS capillary column (30 m \times 0.25 mm \times 0.25 μm); the oven temperature was programmed from an initial temperature of 313 K for 4 min to a final temperature of 513 K for 3 min with a heating rate of 10 K/min.

Continuous-flow experiments. Continuous-flow experiments were performed in a stainless steel fixed-bed continuous-flow reactor with a quartz lining (i.d. = 6 mm). The powder of zeolite H-Y was extruded and sieved into 40-60 mesh. 0.6 Gram of zeolite H-Y was loaded at the central portion in the reactor. Prior to the reaction, zeolite H-Y was activated at 723 K in an Ar flow of 20 mL/min for 60 min to remove water and other adsorbed species. After cooling down to the desired reaction temperature (443-483 K), a mixture gas with $V(\text{C}_2\text{H}_4)/V(\text{Ar}) = 1/11$ was introduced into the reactor. The conversion of ethene was carried out at ambient pressure, $T = 443, 463, \text{ and } 483 \text{ K}$, and $GHSV = 12000 \text{ mL}/(\text{g}_{\text{cat}} \text{ h})$. The lines between the reactor and the valves were heated to 403 K to prevent product condensation. The gaseous effluents were analyzed via an on-line GC (Fuli 9790 II) equipped with a flame ionization detector and an Agilent HP-Plot Q capillary column (30 m \times 0.53 mm \times 40 μm). The zeolite-trapped organics were qualitatively analyzed via an off-line GC-MS analyzer equipped with a DB-5 MS capillary column (30 m \times 0.25 mm \times 0.25 μm). The following equations are used to evaluate the performance of zeolite H-Y.

The C_2H_4 conversion ($X_{\text{C}_2\text{H}_4}$) was calculated based on the difference of C_2H_4 concentration between the inlet ($A_{\text{C}_2\text{H}_4,\text{inlet}}$) and outlet ($A_{\text{C}_2\text{H}_4,\text{outlet}}$).

$$X_{\text{C}_2\text{H}_4} = \frac{A_{\text{C}_2\text{H}_4,\text{inlet}} - A_{\text{C}_2\text{H}_4,\text{outlet}}}{A_{\text{C}_2\text{H}_4,\text{inlet}}} \times 100\%$$

The selectivity of C_nH_m ($S_{\text{C}_n\text{H}_m}$) in the hydrocarbon products was calculated using the following formula:

$$S_{C_nH_m} = \frac{A_{C_nH_m}/n}{\sum A_{C_nH_m}/n} \times 100\%$$

DFT calculations. All DFT calculations were performed within periodic boundary conditions using the Vienna Ab initio Simulation Package (version 5.4.4).¹⁻³ The Perdew-Burke-Ernzerhof (PBE) functional⁴ with projector augmented wave (PAW) method^{5,6} was used. The cut-off energy of the plane wave basis sets was set to 500 eV. The Brillouin zone sampling was restricted to the Γ point.⁷ The dispersion-corrected DFT-D3(BJ) method was used to describe the van der Waals interactions.⁸ The geometry optimizations were assumed to be converged when the force on each atom was below 0.05 eV/Å. The minimum-energy reaction coordinates and transition states were determined using the climbing image nudged elastic band (CI-NEB) method.⁹ The maximum energy geometries along the reaction path from CI-NEB calculations were further optimized by a quasi-Newton algorithm. To obtain more accurate electronic energies, single-point energy calculations were performed using HSE06 hybrid functional¹⁰⁻¹² with D3(BJ) corrections. To calculate Gibbs free energy barriers (G_a), thermal corrections were calculated using statistical thermodynamics, and vibrational components were determined by harmonic frequency calculations (443 K, 0.2 atm).

$$G(T, P) = H - T \times S = E_e + E_{trans} + E_{rot} + E_{vib} + PV - T \times (S_{trans} + S_{rot} + S_{vib})$$

It can be seen that Gibbs free energies (G) include contributions of enthalpy (H) and entropy ($-T \times S$). The translational, rotational, and vibrational enthalpic and entropic contributions of gas-phase molecules were calculated by considering them as ideal gases. It was assumed that three translational and three rotational degrees of freedom are completely lost for alkoxy and ion-pair zeolite structures, while the physisorption of ethene in zeolite was approximated to only lose one translational and two rotational degrees of freedom because the adsorbed ethene still possessed a limited mobility in the pore.^{13,14} These thermal corrections were assisted by VASPKIT 1.2.4.¹⁵ Gibbs free energy barriers (G_a) were then computed using HSE06 single-point energies with thermal corrections.

Zeolite H-Y (FAU topology) was simulated by a rhombohedral 48T unit cell.¹⁶ The Brønsted acid site was introduced by the isomorphous substitution of an Al for lattice Si with charge-compensating proton in the supercage of FAU zeolite (Figure S16). Full geometry optimizations with guest molecules were conducted with fixed lattice parameters ($a = b = c = 17.29 \text{ \AA}$, $\alpha = \beta = \gamma = 60^\circ$).

B. Characterization of zeolite H-Y

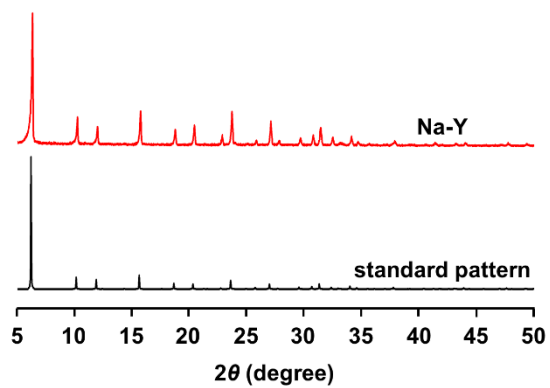


Figure S1. Powder X-ray diffraction pattern for zeolite Na-Y (red) and the standard pattern for the faujasite zeolite (black).

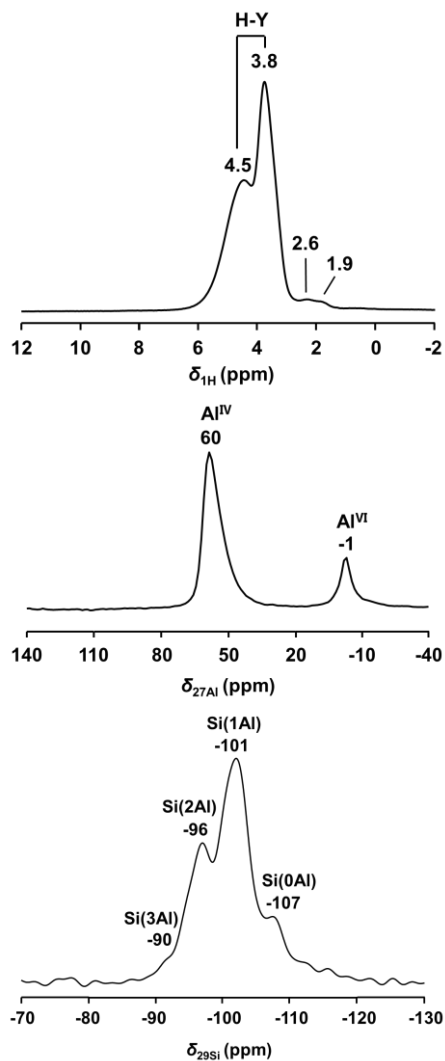


Figure S2. ^1H , ^{27}Al , and ^{29}Si MAS NMR spectra of zeolite H-Y. In the ^1H MAS NMR spectrum, two major signals at 4.5 and 3.8 ppm are assigned for Brønsted acid sites in sodalite cages and supercages, respectively. The minor peaks at 2.6 ppm and 1.9 ppm are attributed to AlOH hydroxyl groups and non-acidic SiOH groups, respectively. In the ^{27}Al MAS NMR spectrum, the signals at 60 and -1 ppm are ascribed to the tetracoordinated and hexacoordinated framework aluminum species, respectively. In the ^{29}Si MAS NMR spectrum, resonances at -90, -96, -101, and -107 ppm can be attributed to the Si(3Al), Si(2Al), Si(1Al), and Si(0Al) sites, respectively. These results indicated that zeolite H-Y obtained after ion-exchange and calcination was neither damaged nor dealuminated.

C. Conversion of ethene on zeolite H-Y

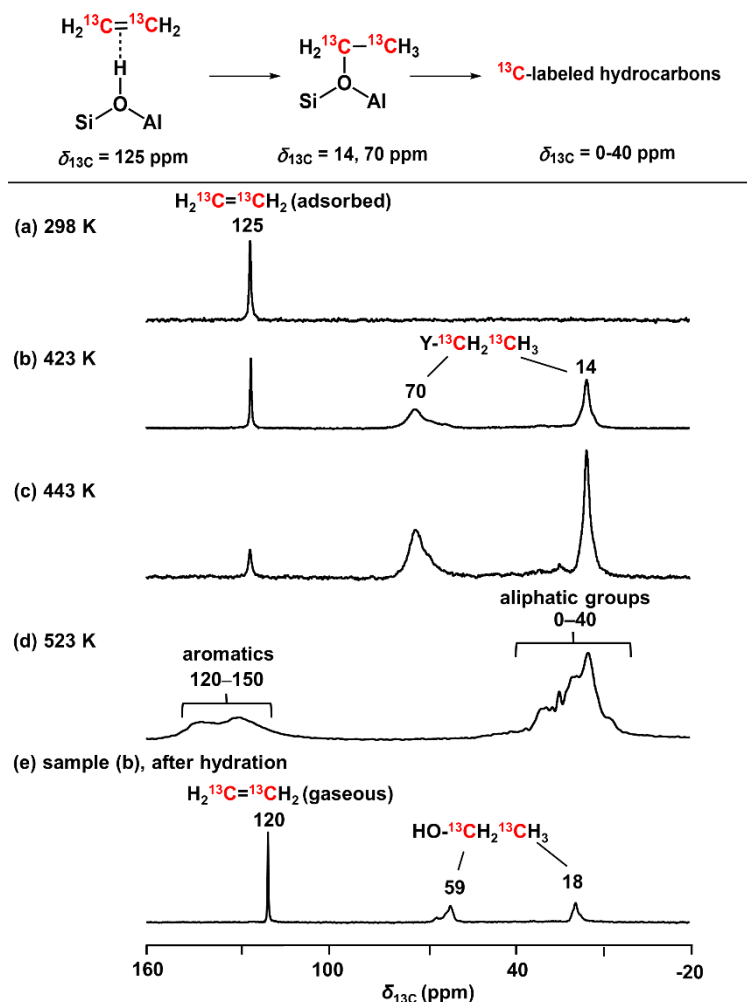
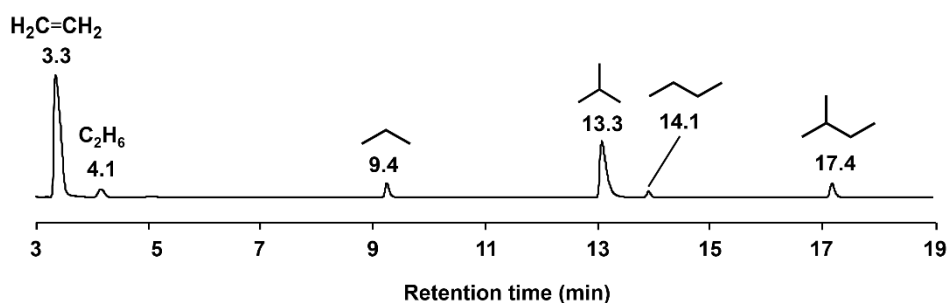


Figure S3. ^{13}C CP MAS NMR spectra recorded after the conversion of ^{13}C -labeled ethene on zeolite H-Y at reaction temperatures of 298 K (a), 423 K (b), 443 K (d), and 523 K (d). The formation of SES is evidenced by the signals occurring at 70 ppm and 14 ppm. These ascriptions are consistent with the reported works. The formation of ethanol via hydration of SES was evidenced by the signals simultaneously occurring at 59 ppm and 18 ppm (e).

D. Identification of hydrocarbon products during conversion of ethene

(a)



(b)

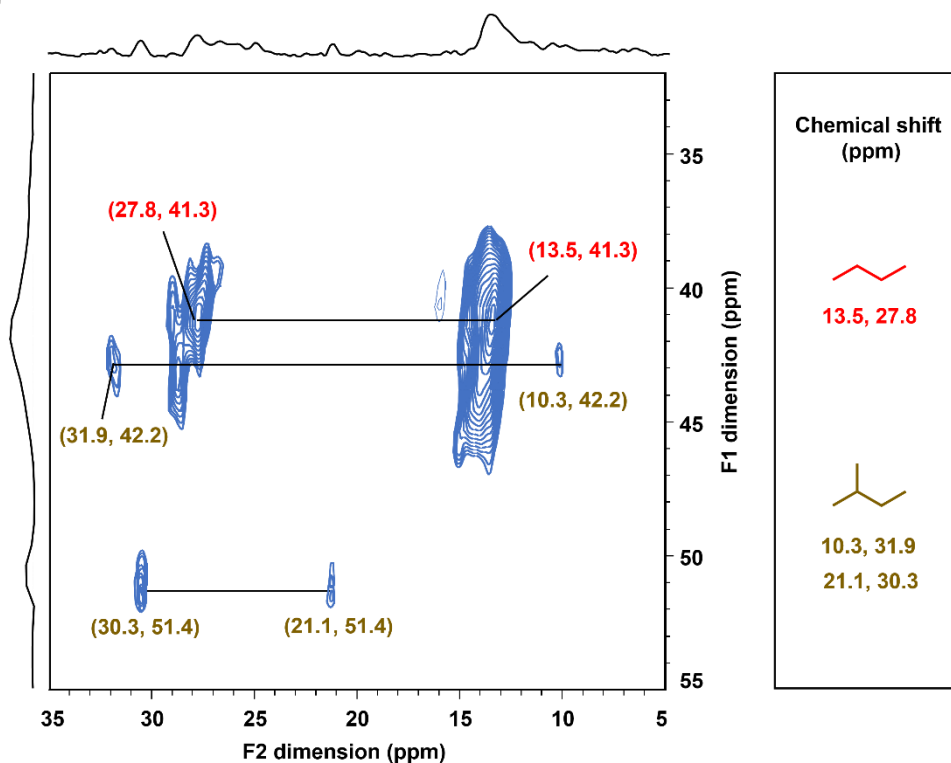


Figure S4. Analysis on the gaseous products obtained from the conversion of ethene over zeolite H-Y. Total ion chromatogram of GC-MS (a) and 2D ¹³C-¹³C INADEQUATE spectrum (b) recorded after conversion of ¹³C-labeled ethene over zeolite H-Y at 523 K for 0.5 h. The gaseous products were identified as C₂-C₅ alkanes. These ascriptions are consistent with the reported works.¹⁷⁻¹⁹

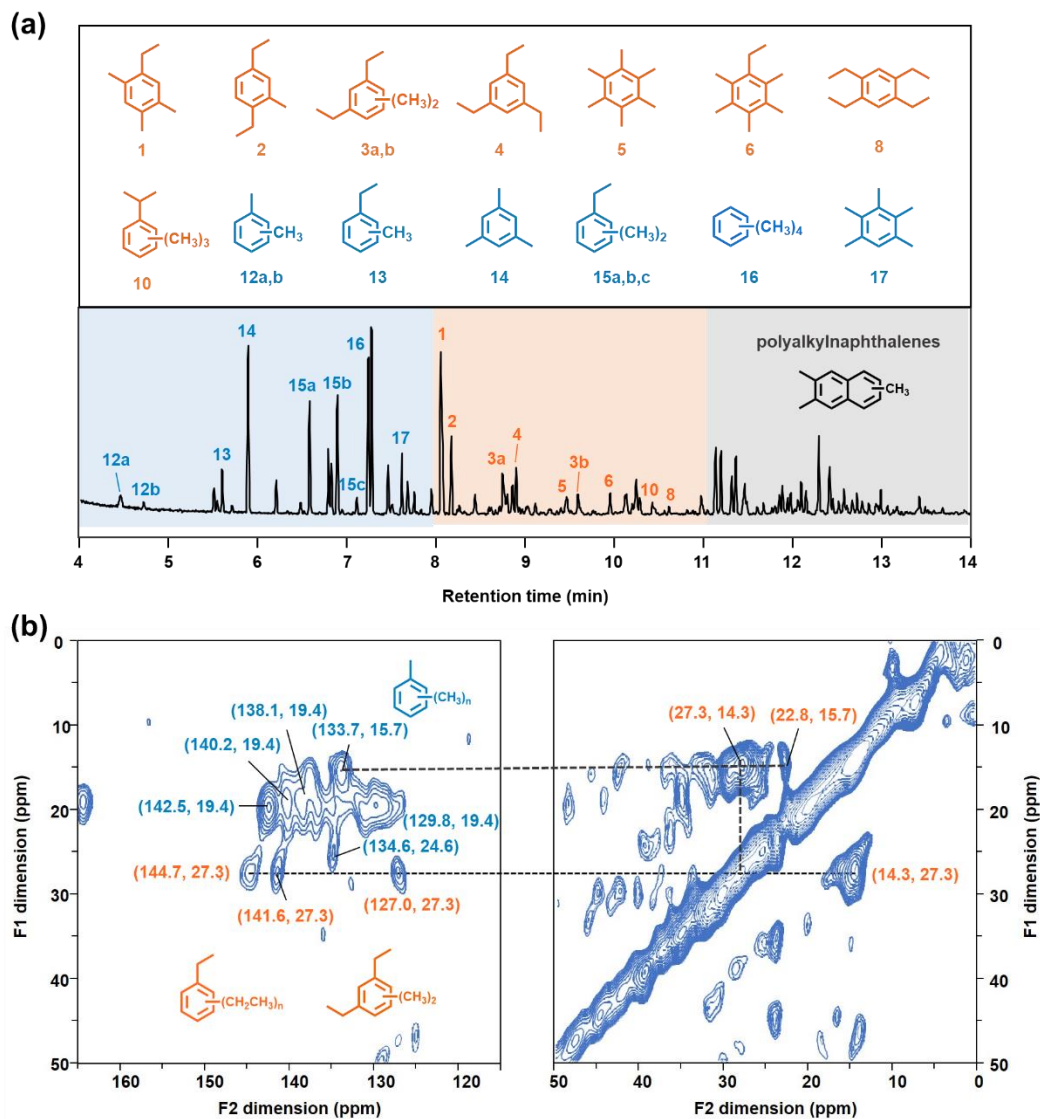


Figure S5. Analysis on zeolite-trapped organics obtained from the conversion of ethene over zeolite H-Y. Total ion chromatogram of GC-MS (a) and 2D ^{13}C - ^{13}C CORD spin diffusion MAS NMR spectra with a mixing time of 50 ms (b) recorded after the conversion of ^{13}C -labeled ethene over zeolite H-Y at 523 K for 0.5 h. The assignments of the peaks in total ion chromatogram of GC-MS were according to the NIST database²⁰. The alkyl-substituted aromatics were identified as zeolite-trapped organic molecules, the assignments of which were in good accordance with the previous work on ethene conversion^{21,22} and ethanol-to-hydrocarbons process^{23,24}.

E. Conversion of ethene on zeolite H-SAPO-34

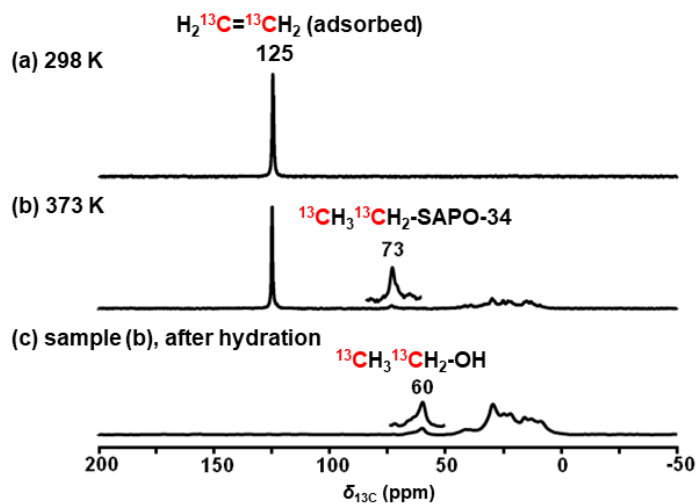


Figure S6. ^{13}C CP MAS NMR spectra recorded after the conversion of ^{13}C -labeled ethene on zeolite H-SAPO-34 at the reaction temperatures of 298 K (a) and 373 K (b). The formation of SES is evidenced by the NMR signal at 73 ppm. The formation of ethanol as the hydration product of SES was evidenced by the signal occurring at 60 ppm (c). Oligomerization of ethene occurred to some extent at 373 K, giving rise to the high-field signals at 0–40 ppm in (b) and (c).

F. Preparation of SES by dehydration of ethanol on zeolite H-Y

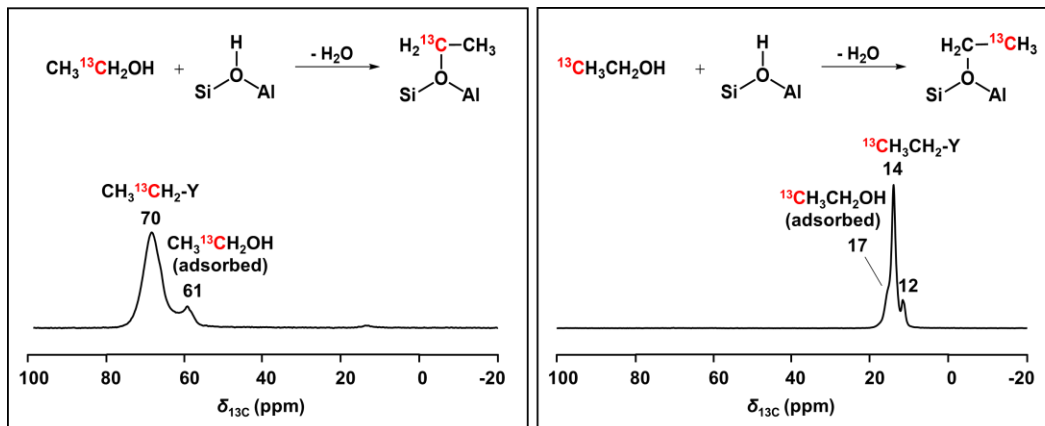


Figure S7. ^{13}C CP MAS NMR spectra of ^{13}C -1-labeled SES ($\text{CH}_3\text{}^{13}\text{CH}_2\text{-Y}$, left) and ^{13}C -2-labeled SES ($^{13}\text{CH}_3\text{CH}_2\text{-Y}$, right) prepared by dehydration of selectively ^{13}C -labeled ethanol on zeolite H-Y. The signal at 70 ppm is attributed to the methylene carbon of $\text{CH}_3\text{}^{13}\text{CH}_2\text{-Y}$, while the signals at 14 and 12 ppm belong to the methyl carbon of $^{13}\text{CH}_3\text{CH}_2\text{-Y}$ at different cages in zeolite H-Y. The signals at 61 and 17 ppm are assigned to adsorbed ethanol.

G. ^{13}C scrambling of SES on zeolite H-Y

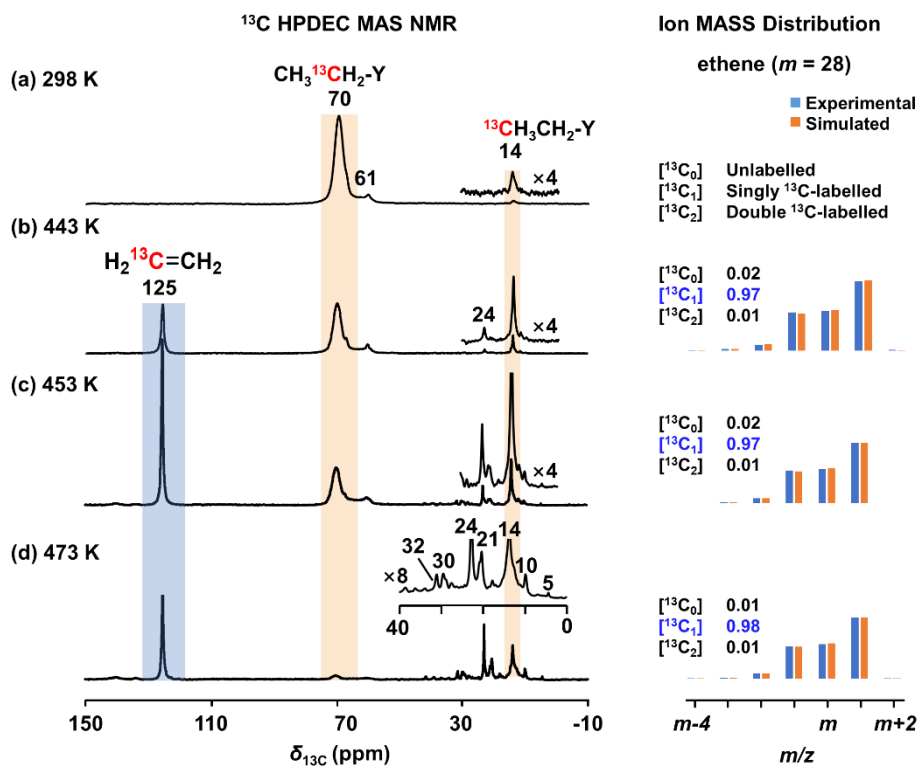
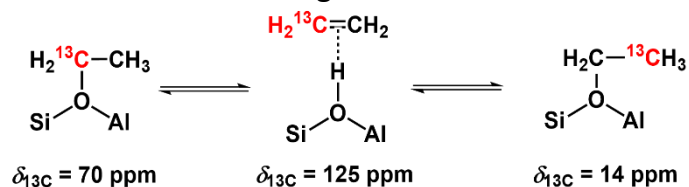


Figure S8. ^{13}C HPDEC MAS NMR spectra (left) and the corresponding bar graphs of mass spectra for ethene in molecular ion region (right) recorded upon the conversion of ^{13}C -1-labelled SES ($\text{CH}_3^{13}\text{CH}_2\text{-Y}$) for 0.5 h at 298 K (a), 443 K (b), 453 K (c), and 473 K (d).

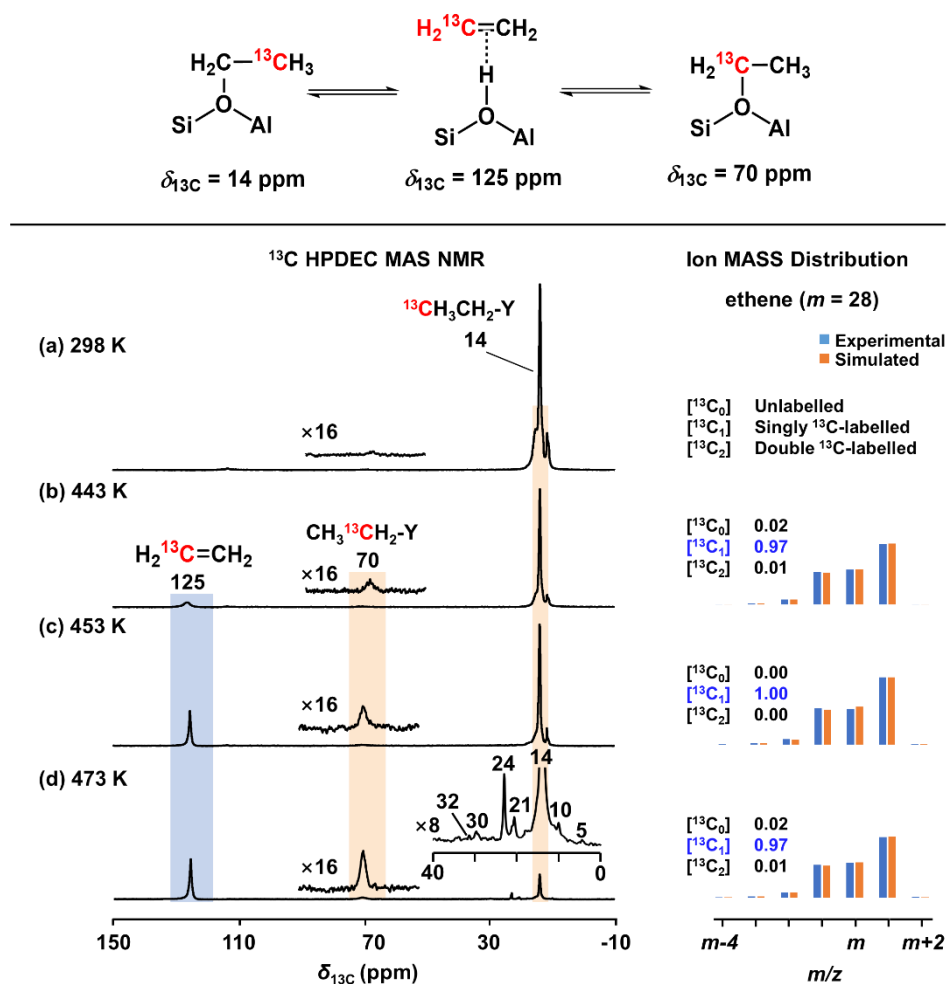


Figure S9. ^{13}C HPDEC MAS NMR spectra (left) and the corresponding bar graphs of mass spectra for ethene in molecular ion region (right) recorded upon the conversion of ^{13}C -2-labeled SES ($^{13}\text{CH}_3\text{CH}_2\text{-Y}$) for 0.5 h at 298 K (a), 443 K (b), 453 K (c), and 473 K (d).

In Figure S8 and Figure S9 were shown the ^{13}C HPDEC MAS NMR spectra recorded upon the transformation of $\text{CH}_3\ ^{13}\text{CH}_2\text{-Y}$ and $^{13}\text{CH}_3\text{CH}_2\text{-Y}$ at $T = 298\text{--}473$ K, respectively. At the temperature of $T = 443\text{--}453$ K (Figures S8b–c and S9b–c), accompanied by the formation of ethene (^{13}C NMR signal at $\delta = 125$ ppm), the ^{13}C scrambling between methylene (^{13}C NMR signal at $\delta = 70$ ppm) and methyl (^{13}C NMR signal at $\delta = 14$ ppm) carbons of SES was observed. These observations are consistent with the results obtained from the ^{13}C CP MAS NMR spectra (Figure 2 in the main text). The fitted GC–MS results showed that ethene was almost singly ^{13}C -labelled, indicating that ethene was derived from the deprotonation of singly ^{13}C -labelled SES. At a higher temperature of $T = 473$ K (Figures S8d and S9d), the products were identified as ethene, ethane, propane, isobutane, *n*-butane, and isopentane, which were in good accordance with those for the products of ethene conversion in Figure S4.

H. ^{13}C isotopic distributions in $\text{C}_2\text{--C}_5$ hydrocarbons

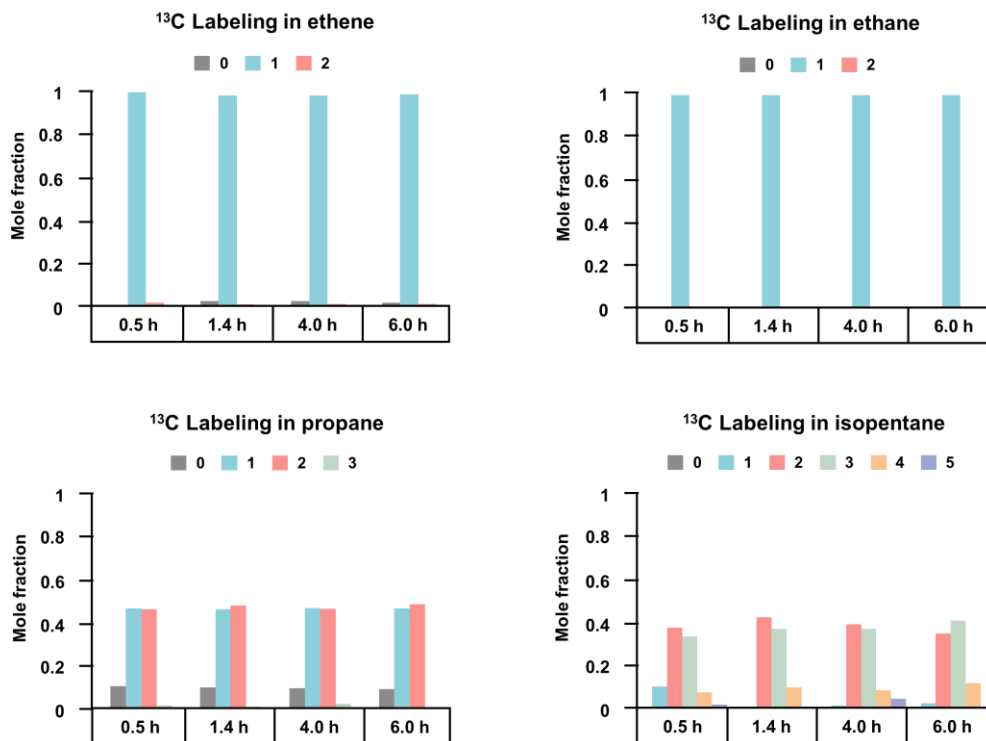


Figure S10. ^{13}C isotopic distributions for ethene, ethane, propane, and isopentane recorded after the conversion of ^{13}C -1-labeled SES ($\text{CH}_3^{13}\text{CH}_2\text{-Y}$) at 443 K for 0.5 h, 1.4 h, 4.0 h, and 6.0 h. The numbers 0–5 represent the number of ^{13}C atoms incorporated in the products.

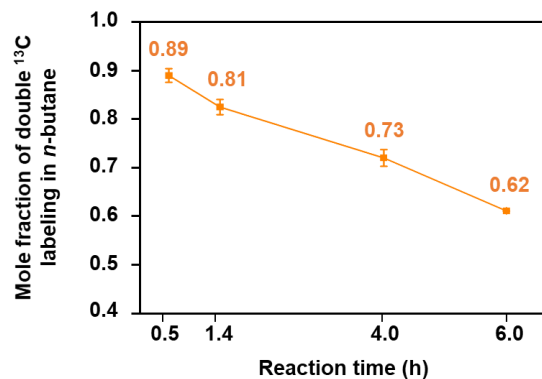


Figure S11. Mole fraction of double ^{13}C labeling in n -butane obtained from the decomposition of ^{13}C -1-labeled SES ($\text{CH}_3^{13}\text{CH}_2\text{-Y}$) at 443 K for 0.5 h, 1.4 h, 4.0 h, and 6.0 h.

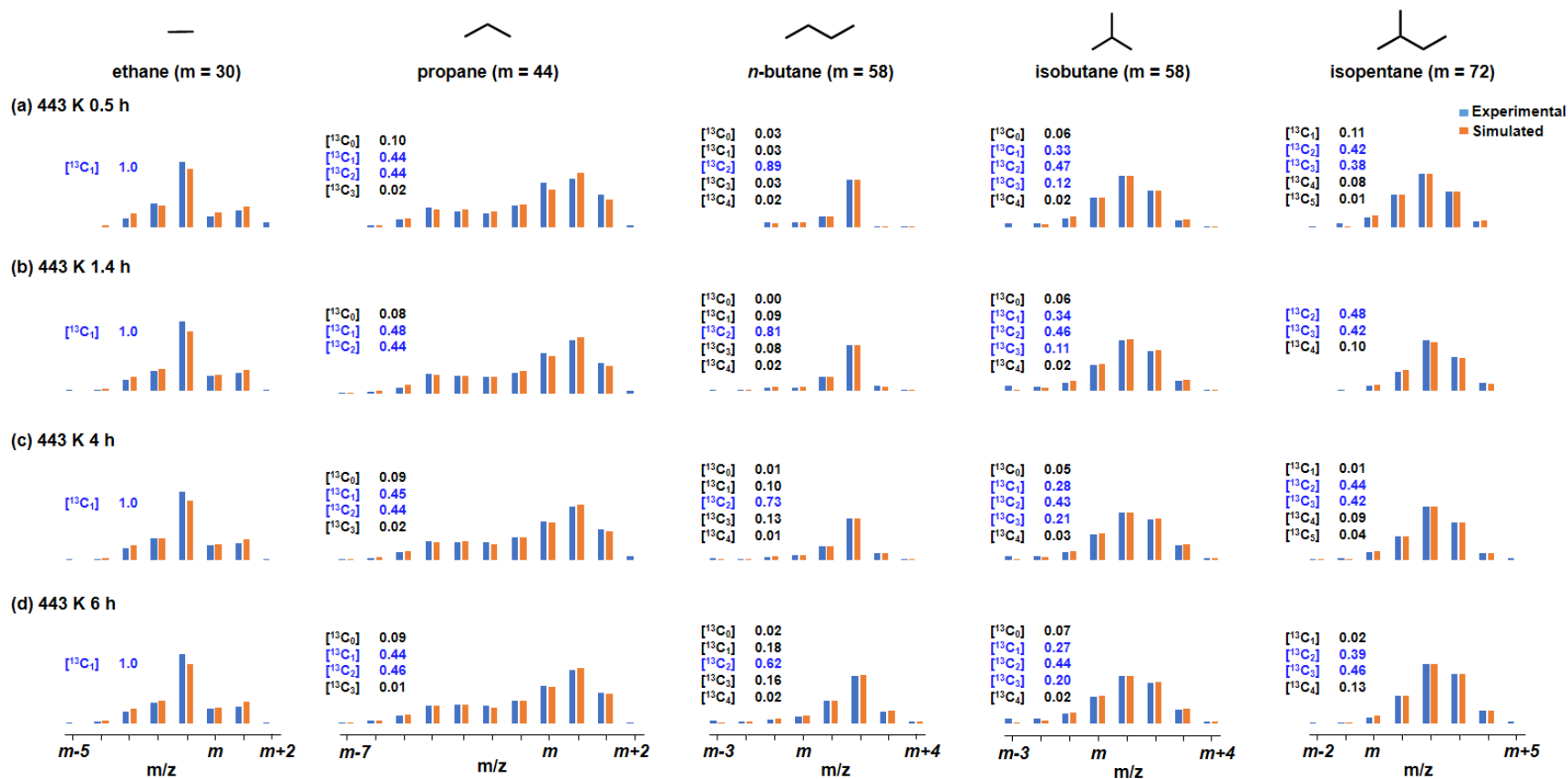


Figure S12. The bar graphs of mass spectra for ethane, propane, *n*-butane, isobutane, and isopentane in the molecular ion region, recorded after the conversion of ¹³C-1-labeled SES (CH₃¹³CH₂-Y) at 443 K for 0.5 h (a), 1.4 h (b), 4.0 h (c), and 6.0 h (d). The mole fractions of ¹³C isotopic isomers in each product (donated as [¹³C_n]) were obtained by the simulation of isotope distribution patterns. The experimental ion mass distributions of ¹³C-labeled products were fitted by the solver function of Microsoft Excel 2016.

I. Analysis of zeolite-trapped organics after decomposition of SES

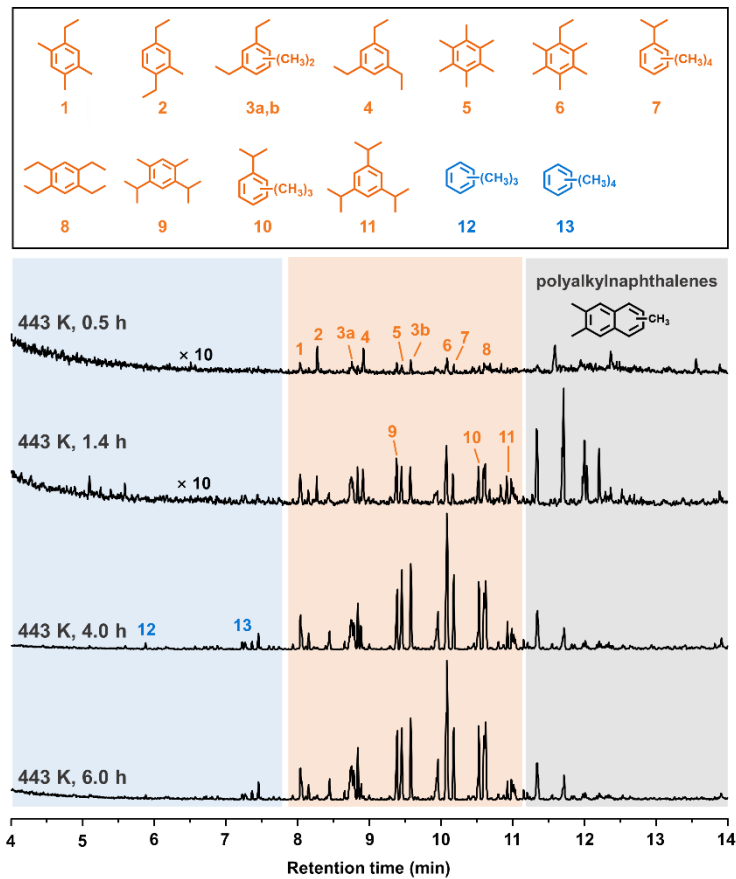


Figure S13. GC–MS analysis on zeolite-trapped components obtained from the decomposition of ^{13}C -1-labeled SES ($\text{CH}_3^{13}\text{CH}_2\text{-Y}$) at 443 K for 0.5–6.0 h. The alkyl-substituted aromatics were identified as zeolite-trapped organic species.

J. Continuous-flow experiments for conversion of ethene on zeolite H-Y

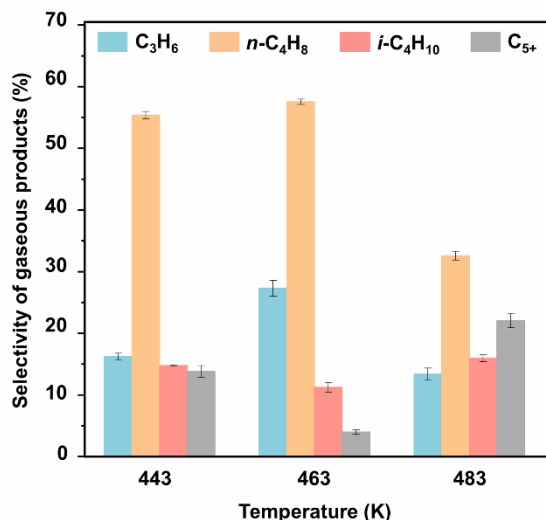


Figure S14. Selectivity of gaseous products analyzed by on-line GC upon the conversion of ethene on zeolite H-Y within a plug flow reactor at the reaction temperatures of $T = 443, 463,$ and 483 K. Reaction conditions: $P =$ ambient pressure, $V(\text{C}_2\text{H}_4)/V(\text{Ar}) = 1/11$, $GHSV = 12000$ mL/(g_{cat} h), and ethene conversion $< 5\%$. The error bar on each data point represents the standard deviation associated with each measurement. The mean value and the standard deviation were calculated by the descriptive statistics in Origin 2023. These data, indicated that *n*-butenes were the main gaseous products at low ethene conversion, in agreement with the results reported in the literature²⁵.

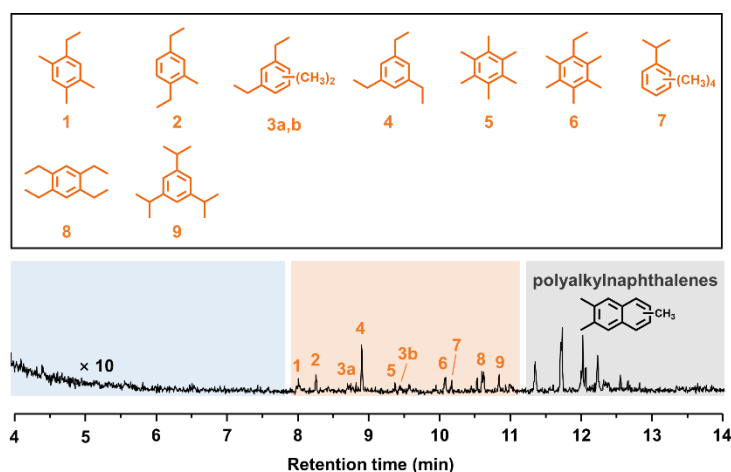
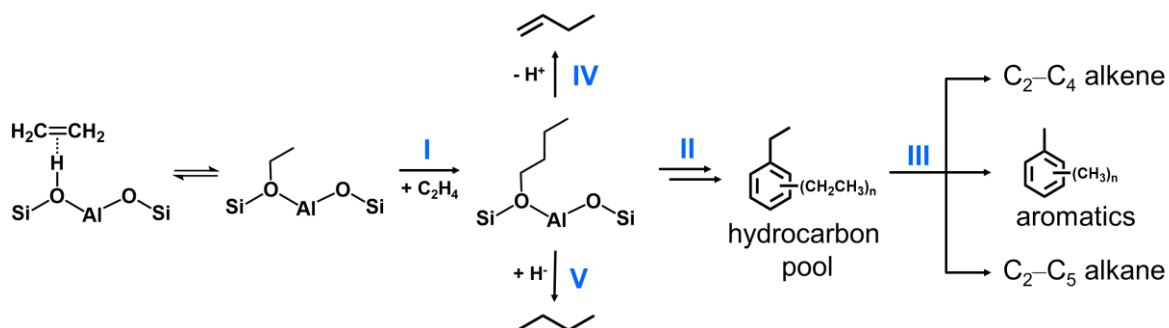


Figure S15. GC-MS analysis on zeolite-trapped components after the conversion of ethene on zeolite H-Y within a plug flow reactor at 463 K. Reaction conditions: $P =$ ambient pressure, $V(\text{C}_2\text{H}_4)/V(\text{Ar}) = 1/11$, $GHSV = 12000$ mL/(g_{cat} h), and ethene conversion $< 5\%$. The assignments of these peaks as alkyl-substituted aromatics were according to the NIST database²⁰.

K. Overall mechanism for conversion of ethene to hydrocarbons



Scheme S1. The mechanism proposed for the conversion of ethene to hydrocarbons.

Based on the product distribution (presented in Sections D and J) and hydrocarbon pool mechanism documented in the literature^{21–30}, the conversion of ethene to hydrocarbons is proposed to involve three consecutive stages (Scheme S1): the first being the generation of surface n -butoxy species via ethylation of ethene by SES (Route I), followed by the formation of hydrocarbon pool species (alkyl-substituted aromatics) via alkylation/cyclization (Route II). Subsequently, the hydrocarbon pool species could result in the production of $\text{C}_2\text{-C}_4$ alkenes, aromatics and $\text{C}_2\text{-C}_5$ alkanes (Route III). Indeed, our ssNMR and GC-MS investigations have confirmed the formation of $\text{C}_2\text{-C}_5$ alkanes and aromatics; while the continuous-flow experiments have verified the formation of $\text{C}_2\text{-C}_4$ alkenes and aromatics. These observations are also in agreement with the information reported in the literature.^{22–25}

Several research groups^{21–23,25,28} have observed the formation of n -butenes in the initial stage of ethene conversion, suggesting that n -butenes are formed by the deprotonation of surface n -butoxy species (Route IV). In this work, the isotopic tracer experiments on the transformation of selectively ^{13}C -labeled SES further confirmed n -butane as the initial C_4 product formed by hydride transfer to surface n -butoxy species (Route V).

L. DFT study on conversion of ethene into surface *n*-butoxy species

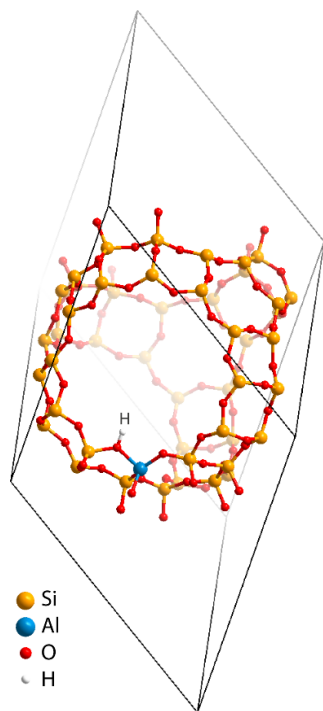


Figure S16. Computational model of zeolite H-Y ($\text{Si}_{47}\text{AlO}_{96}\text{H}$).

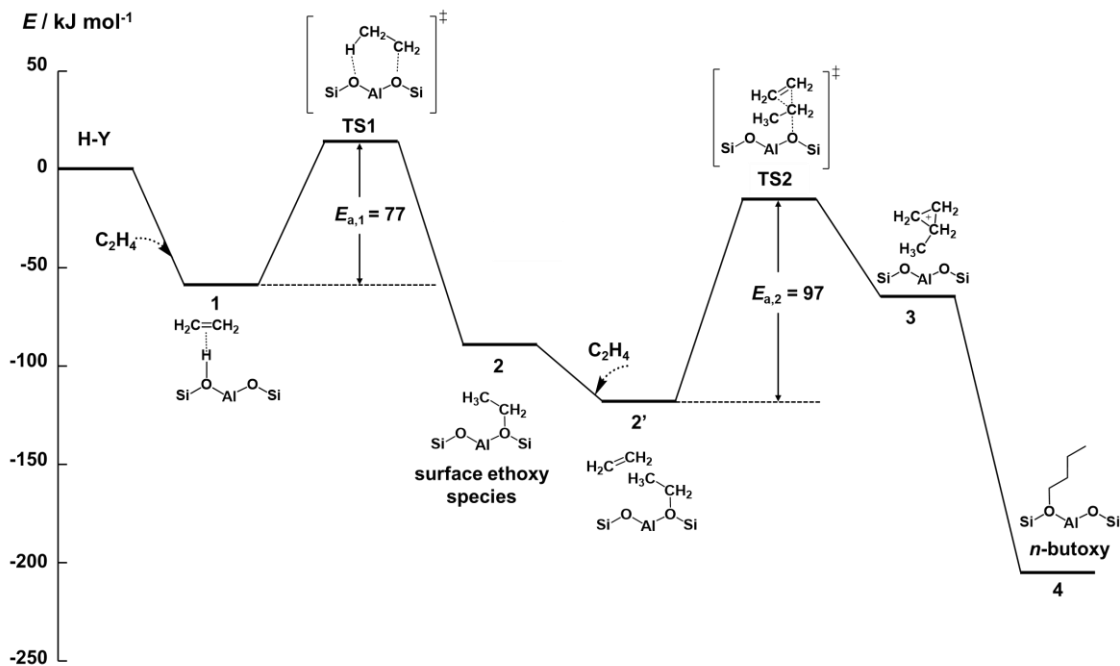


Figure S17. Reaction energy profile for conversion of ethene to surface *n*-butoxy species via the stepwise mechanism, which involves SES as the reactive intermediates. The relative energies are given from the level of PBE-D3(BJ) calculations.

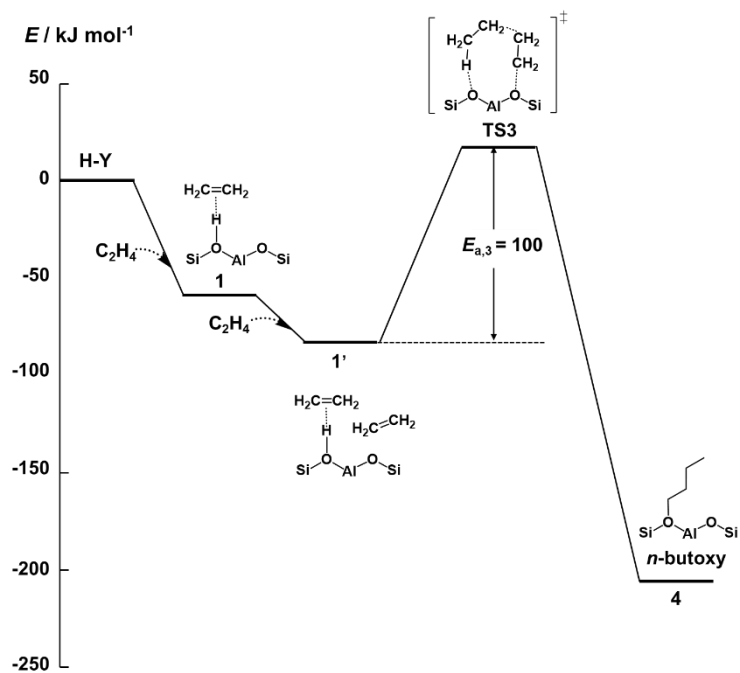


Figure S18. Reaction energy profile for conversion of ethene to surface *n*-butoxy species via the concerted mechanism. The relative energies are given from the level of PBE-D3(BJ) calculations.

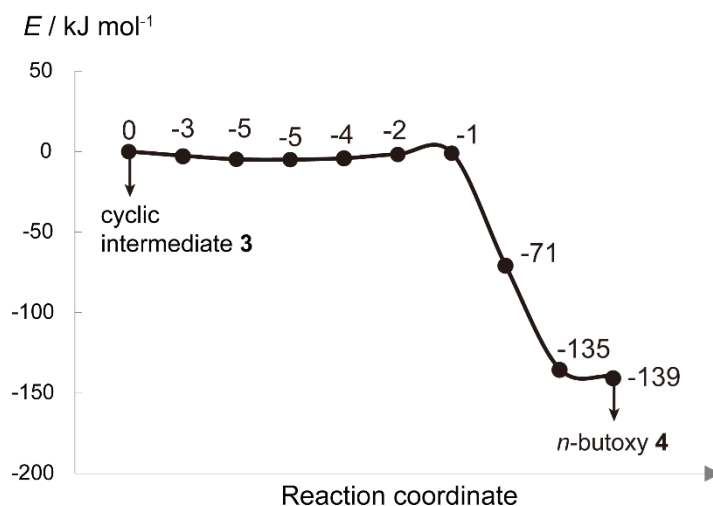


Figure S19. Minimum-energy reaction paths of the metastable cyclic intermediate **3** to surface *n*-butoxy species **4** determined by CI-NEB calculations. The relative energies (PBE-D3(BJ)) are given for the CI-NEB images along the reaction paths.

To better understand the role of SES for the formation of *n*-butane, the DFT optimizations were performed at the level of PBE-D3(BJ) calculations. To account for the effect of zeolite micropore dimension, zeolite H-Y was simulated by a periodic 48T unit cell (Figure S16). Two possible reaction mechanisms for conversion of ethene into surface *n*-butoxy species on zeolite H-Y were investigated: stepwise mechanism and concerted mechanism. The respective energy profiles and activation barriers (E_a) are shown in Figures S17 and S18. In the stepwise mechanism (Figure S17), the protonation of one ethene **1** first occurs to form SES **2** (TS1, $E_{a,1} = 77 \text{ kJ mol}^{-1}$). Then, SES **2** react with the second adsorbed ethene (TS2, $E_{a,2} = 97 \text{ kJ mol}^{-1}$) to afford a metastable cyclic intermediate **3** which resembles the structure of protonated methylcyclopropane. Minimum-energy reaction paths calculations (Figure S19) suggest that cyclic intermediate **3** is readily converted to surface *n*-butoxy species **4** with negligible activation barriers. In the concerted mechanism (Figure S18), the transformation of two ethene occurs in one single-step via (TS3, $E_{a,3} = 100 \text{ kJ mol}^{-1}$), which yields C₄ alkoxy in the form of surface *n*-butoxy species **4**. Based on the PBE-optimized structures, single-point energy calculations using HSE06 hybrid functional were performed to obtain more accurate electronic energies. The comparison of E_a (HSE06) and E_a (PBE) (Table S1) suggests that the PBE functional calculations underestimate E_a values but do not affect the trend of $E_{a,1}$, $E_{a,2}$, and $E_{a,3}$, in which the activation barrier for SES formation from ethene $E_{a,1}$ is the lowest.

In order to take the reaction conditions into consideration and to properly distinguish the competitive reaction pathways, the Gibbs free energies at $T = 443 \text{ K}$ and $P = 0.2 \text{ atm}$ were calculated from harmonic frequencies. The inclusion of both enthalpy effect and entropy effect shows that the Gibbs free energy

barriers for the stepwise mechanism with $G_{a,1} = 145 \text{ kJ mol}^{-1}$ (**1** \rightarrow **2**) and $G_{a,2} = 170 \text{ kJ mol}^{-1}$ (**2** \rightarrow **3**) are significantly lower than that for the concerted mechanism with $G_{a,3} = 205 \text{ kJ mol}^{-1}$ (**1** \rightarrow **4**), suggesting that ethene ethylation to surface *n*-butoxy species via the stepwise mechanism is more plausible. The comparison of enthalpic (H_a) and entropic ($-T \times S_a$) contributions for the two mechanisms suggests that the preference of stepwise over concerted mechanism is mainly contributed from the entropy effect. Compared with the stepwise mechanism in which one ethene is converted to surface alkoxy species in each step (TS1 and TS2), the concerted mechanism requires two ethene to be restricted over Brønsted acid site in one single step (TS3), and thus the effect of entropy decrease in TS3 is more significant, which leads to a much stronger increase of $G_{a,3}$ than $G_{a,1}$ and $G_{a,2}$.

Based on the above results, we finally emphasized the formation of SES and its role in the initial stage of ethene conversion over zeolite H-Y. The formation of C-C bonds from adsorbed ethene to yield C_4 species could occur through either the stepwise mechanism mediated by SES or the concerted mechanism. The energy change from adsorbed ethene to SES (**1** \rightarrow **2**) is -42 kJ mol^{-1} at HSE06 level, and the inclusion of Gibbs free energy corrections give an energy change of $+22 \text{ kJ mol}^{-1}$ due to a much stronger entropy loss in SES than in the adsorbed ethene. The reverse reaction (**2** \rightarrow **1**) may also occur with a G_a of 123 kJ mol^{-1} , leading to an equilibrium between adsorbed ethene and SES which is dependent on the reaction conditions. The SES may either react with ethene to produce C_4 species or decompose back as ethene. DFT data suggest that the stepwise and concerted mechanisms require maximum Gibbs free energy barriers of 170 and 205 kJ mol^{-1} , respectively, and thus stepwise mechanism is more favorable. We suggest that SES play the crucial role as a relatively stable intermediate, offering a lower energy pathway for the formation of C-C bond in C_4 species.

Table S1. Calculated free energy barriers (G_a), the enthalpic (H_a) and entropic ($-T \times S_a$) contributions for conversion of ethene to surface *n*-butoxy species via the stepwise (TS1 and TS2) and concerted (TS3) pathways. E_a (PBE) and E_a (HSE06) are activation barriers from the PBE optimizations and HSE06 single-point energy calculations, respectively. All energies are computed with D3(BJ) dispersion corrections and are given in the unit of kJ mol^{-1} .

No.	Reaction steps	E_a (PBE)	E_a (HSE06)	G_a	H_a	$-T \times S_a$
1	1 \rightarrow 2 (TS1)	77	94	145	88	57
2	2 \rightarrow 3 (TS2)	97	119	170	127	43
3	1 \rightarrow 4 (TS3)	100	122	205	121	84

M. References

- 1 G. Kresse and J. Hafner, *Phys. Rev. B*, 1993, **48**, 13115–13118.
- 2 G. Kresse and J. Hafner, *Phys. Rev. B*, 1994, **49**, 14251–14269.
- 3 G. Kresse and J. Furthmüller, *Comput. Mater. Sci.*, 1996, **6**, 15–50.
- 4 J. P. Perdew, K. Burke and M. Ernzerhof, *Phys. Rev. Lett.*, 1996, **77**, 3865–3868.
- 5 P. E. Blöchl, *Phys. Rev. B*, 1994, **50**, 17953–17979.
- 6 G. Kresse and D. Joubert, *Phys. Rev. B*, 1999, **59**, 1758–1775.
- 7 J. D. Pack and H. J. Monkhorst, *Phys. Rev. B*, 1977, **16**, 1748–1749.
- 8 S. Grimme, S. Ehrlich and L. Goerigk, *J. Comput. Chem.*, 2011, **32**, 1456–1465.
- 9 G. Henkelman and H. Jónsson, *J. Chem. Phys.*, 2000, **113**, 9978–9985.
- 10 J. Heyd, G. E. Scuseria and M. Ernzerhof, *J. Chem. Phys.*, 2003, **118**, 8207–8215.
- 11 J. Heyd and G. E. Scuseria, *J. Chem. Phys.*, 2004, **121**, 1187–1192.
- 12 A. V. Krukau, O. A. Vydrov, A. F. Izmaylov and G. E. Scuseria, *J. Chem. Phys.*, 2006, **125**, 224106–224110.
- 13 B. A. De Moor, M. Reyniers and G. B. Marin, *Phys. Chem. Chem. Phys.*, 2009, **11**, 2939–2958.
- 14 B. A. De Moor, A. Ghysels, M. Reyniers, V. Van Speybroeck, M. Waroquier and G. B. Marin, *J. Chem. Theory Comput.*, 2011, **7**, 1090–1101.
- 15 V. Wang, N. Xu, J. Liu, G. Tang and W. Geng, *Comput. Phys. Commun.*, 2021, **267**, 108033–108051.
- 16 J. A. Hriljac, M. M. Eddy, A. K. Cheetham, J. A. Donohue and G. J. Ray, *J. Solid State Chem.*, 1993, **106**, 66–72.
- 17 E. G. Dreouane, C. Lefebvre and J. B. Nagy, *J. Mol. Catal.*, 1986, **38**, 387–391.
- 18 I. Ivanova, E. B. Pomakhina, A. I. Rebrov and E. G. Derouane, *Top. Catal.*, 1998, **6**, 49–59.
- 19 M. V. Luzgin, A. G. Stepanov, S. S. Arzumanov, V. A. Rogov, V. N. Parmon, W. Wang, M. Hunger and D. Freude, *Chem. Eur. J.*, 2006, **12**, 457–465.
- 20 NIST Chemistry Web book. <http://webbook.nist.gov/chemistry>
- 21 K. Lee and S. B. Hong, *ACS Catal.*, 2019, **9**, 10640–10648.
- 22 H. Wang, Y. Hou, W. Sun, Q. Hu, H. Xiong, T. Wang, B. Yan and W. Qian, *ACS Catal.*, 2020, **10**, 5288–5298.
- 23 A. D. Chowdhury, A. L. Paioni, G. T. Whiting, D. Fu, M. Baldus and B. M. Weckhuysen, *Angew. Chem. Int. Ed.*, 2019, **58**, 3908–3912.
- 24 S. Zeng, W. Zhang, J. Li, S. Lin, S. Xu, Y. Wei and Z. Liu, *J. Catal.*, 2022, **413**, 517–526.
- 25 W. Dai, X. Sun, B. Tang, G. Wu, L. Li, N. Guan and M. Hunger, *J. Catal.*, 2014, **314**, 10–20.
- 26 E. A. Uslamin, H. Saito, N. Kosinov, E. Pidko, Y. Sekine and E. J. M. Hensen, *Catal. Sci. Technol.*, 2020, **10**, 2774–2785.
- 27 S. Zeng, J. Li, N. Wang, W. Zhang, Y. Wei, Z. Liu and S. Xu, *Energy & Fuels*, 2021, **35**, 12319–12328.
- 28 H. Oikawa, Y. Shibata, K. Inazu, Y. Iwase, K. Murai, S. Hyodo, G. Kobayashi and T. Baba, *Appl. Catal., A*, 2006, **312**, 181–185.
- 29 R. Batchu, V. V. Galvita, K. Alexopoulos, K. Van der Borght, H. Poelman, M.-F. Reyniers and G. B. Marin, *Appl. Catal., A*, 2017, **538**, 207–220.
- 30 G. Chen, H. Liu, S. Fadaeayerani, J. Shan, A. Xing, J. Cheng, H. Wang and Y. Xiang, *Catal. Sci. Technol.*, 2020, **10**, 4019–4029.